Supplementary Materials

Strong pre-melting effect in the elastic properties of hcp-Fe under inner-core conditions

Benjamí Martorell*, Lidunka Vočadlo, John Brodholt, Ian G. Wood

Department of Earth Sciences, University College London, Gower Street, London, WC1E 6BT, United Kingdom.

*correspondence to: b.massip@ucl.ac.uk

This PDF file includes:

> Methods
> Supplementary Text
> Equations S1 to S6
> Figs. S1 to Sx
> Tables S1

Methods

<u>Electronic</u> <u>Structure</u> <u>Calculations</u>

The calculations performed in this work are based on density functional theory (DFT) using the Vienna Ab Initio Simulation Package (VASP) (*33-35*). To solve the Kohn-Sham equations, this code makes use of a development of the one-electron wave function in a basis of plane waves. The effect of the core electrons on the valence electrons is described by the projector augmented wave method (PAW) (*36,37*). The generalized gradient approximation (GGA) was used with the functional of Perdew and Wang (*38*). A convergence of the plane-wave expansion was obtained with a cut-off of 400 eV.

We ran finite temperature *ab initio* molecular dynamics (AIMD). The VASP code uses the Verlet algorithm to integrate the classical Newton's equations of motion. A time step of 1.5 fs was used for the integration. Simulations were performed at constant temperature using an Andersen thermostat, with a restarting value of 150 cycles.

The simulation box for the pure hcp-Fe was the same as used previously (*9*) to determine the elastic constants of pure hcp-Fe iron. This consisted of a 4x2x2 supercell of the 4-atom C-centred crystallographic cell of the hcp structure with orthogonal axes. A k-points grid of 4 irreducible k-points was used.

Simulations were performed at nominal temperatures of 6500, 7000, 7250, 7500, and 8000 K since results for lower temperatures had already been obtained (*9*). Simulations were run for between 10 and 15 ps. The actual temperature of the simulation was determined from an average excluding the first 2 ps of the simulation. Stresses were determined as outlined below. To ensure that we were computing the stresses of solid phases, we retrieved the radial distribution function (RDF) and the root-mean-square displacements (RMSD) for the last 3.5 ps of each simulation.

<u>Elastic</u> <u>Properties</u>

In order to obtain the elastic properties at 360 GPa we used the same procedure as before (*9*). In summary, we first optimised the unit-cell parameters using VASP-NPT simulations for the isothermal-isobaric ensemble using the barostat implemented in VASP by Hernández (*39,40*); we ran this simulation for up to 5 ps. The average lattice parameters from these NPT simulations were then used to create a unit cell to which distortions were applied (see below); the stresses on the simulation box were then obtained from VASP-NVT simulations run over ~10 ps (for simulations at target temperatures of 7000 and 7500 K, 15 ps were used to ensure convergence).

Once the equilibrium structure of each system was obtained, the elastic constants, c_{ij}, were evaluated by distorting the unit cells according to the two distortion matrices shown below:

$$\begin{pmatrix} 1+\delta & 0 & 0 \\ 0 & \sqrt{3} & \delta\sqrt{3} \\ 0 & \delta\left(\dfrac{c}{a}\right) & \left(\dfrac{c}{a}\right) \end{pmatrix} \text{ and } \begin{pmatrix} 1 & 0 & 0 \\ 0 & \sqrt{3} & 0 \\ 0 & 0 & \left(\dfrac{c}{a}\right)(1+\delta) \end{pmatrix}$$

Within the Voigt average (*9,41*) the elastic properties (incompressibility: K; shear modulus: G) are given by:

$$K_T = \frac{2(c_{11}+c_{12})+4c_{13}+c_{33}}{9} \;\; ; \;\; G = \frac{12c_{44}+7c_{11}-5c_{12}+2c_{33}-4c_{13}}{30}$$

Equation S1

Finally, we obtained the adiabatic incompressibility, K_S, from the relation

$$K_s = K_T(1 + \alpha\gamma T)$$

using values of the volumetric thermal expansion coefficient, $\alpha = 10^{-5}$ K^{-1} and the Grüneisen parameter, $\gamma = 1.5$ (e.g., ref. *4,42*).

The isotropic wave propagation velocities in the material can then be evaluated from the bulk and shear moduli, and the density, ρ, as follows:

$$V_p = \sqrt{\frac{K+\frac{4}{3}G}{\rho}} \;\; ; \;\; V_s = \sqrt{\frac{G}{\rho}}$$

Equation S2

Temperature dependence of the shear modulus and estimate of melting temperature

We used the Nadal-Le Poac (NP) shear modulus model, based on Lindemann melting theory, to describe the temperature dependence of G at a fixed pressure (*13*). This takes the form:

$$G(P,T) = \frac{1}{J(T)}\left[\left(G_0 + \frac{\partial G}{\partial P}\frac{P}{\sqrt[3]{\eta}}\right)\left(1 - \frac{T}{T_m}\right) + \frac{\rho}{Cm}k_b T\right]$$

Equation S3

where

$$C = \frac{(6\pi)^{2/3}}{3}f^2$$

Equation S4

$$J(T) = 1 + exp\left[-\frac{1+\frac{1}{\varsigma}}{1+\varsigma/1-\frac{T}{T_m}}\right]$$

Equation S5

and

$$G_P = G_0 + \frac{\partial G}{\partial P}\frac{P}{\sqrt[3]{\eta}}$$

Equation S6

In Eqs 3-6, G is the shear modulus, P is pressure, T is temperature, G_0 is the shear modulus at 0 K and 0 GPa, η is the compression, T_m is the melting temperature, ρ is the density, m is the atomic mass, k_b is the Boltzmann constant, f is the Lindemann constant for the material and ζ is a material parameter. We have fitted our results to this model with 4 adjustable parameters, i.e., C, ζ, T_m, and G_P (we note that, within the model, ∂G/∂P and η are assumed to be temperature independent and, since our calculations are at constant P, G_P may be taken as a constant). With this model we can obtain the melting temperature of the material and its Lindemann constant. This last value is in the range of 0.1-0.3 for most materials.

Supplementary Text

Root-Mean-Square Displacement and Radial Distribution Function

As stated in main text, we performed RMSD and RDF analysis to discern between solid and liquid structures and confirm that simulated structures at 7350 K or below were solids. At 7350 K and below, RMSD (Fig. S1A) shows the typical behavior for solids, i.e. an almost oscillating behavior around a constant value with simulation time. In contrast, beyond the melting point, at 8000 K, hcp-Fe shows a RMSD increasing with time, the expected behavior for liquids. This is confirmed by the RDF (Fig S1B). At 7350 K and below, two well-defined peaks for the first and second coordination shells exists at 2.1 and 3.3 Å. At 8000 K, the peak of the second coordination shell at 3.3 Å is lost, as expected in liquids, since no long-range order exists.

Atomic Defects Before and After Melting

Atomic defects are a good indicator of how close the system is from melting and how the melt propagates into the solid structure (*27-31*); the percentage of defects increases in the solid structure with temperatures up to 40%, where a collapse in the solid structure occurs and it melts. After this point, the percentage of defects increases substantially to 70% or 80%.

The procedure to evaluate the number of defects is the same as that presented in previous papers (27-31). A defect is defined as an over- or under-coordinated atom (coordination number different to 12 in the first shell). The first coordination shell is formed by those atoms closer to the atomic center than the first minimum in the RDF, i.e., those atoms closer to the atomic center than 1.21 times the average interatomic distance (first maximum in the RDF). After counting all defective atoms in a time step, we averaged that number for the last 5 ps of simulation. The final values show that hcp-Fe is a solid at 7350 K and below, and liquid at 8000 K. (Fig. S3).

Simulation Temperature

We set the thermostat at a nominal, starting temperature, as explained in the Methods section. We checked the temperature at the end of every simulation and we took the time-averaged temperature for each simulation and the standard deviation. That final value is the simulation temperature we give in the paper.

The statistical error is evaluated using the blocking method for correlated data (*43*). The standard deviation is defined as:

$$\sigma \approx \sqrt{\frac{c_0'}{n'-1}\left(1+\frac{1}{\sqrt{2(n'-1)}}\right)}$$

$$n' = \frac{1}{2}n$$

$$x_i' = \frac{1}{2}(x_{2i-1} + x_{2i})$$

$$c_0' = \frac{1}{n'}\sum_{k=1}^{n'}(x_k - \bar{x})^2$$

where a new set of n' data is created to evaluate the minimum standard deviation for this method. After the standard deviation was obtained, we applied a t-student test (we take t=3 for n=∞ and 99.9% of confidence). The final statistic error in temperature goes from ±10 to ±40 K when the temperature increases from 2000 to 8000K, this represents in all cases an error of 0.5% in the temperature determination.

Fig. S1. Root-Mean-Square Displacement (A) and Radial Distribution Function (B) analysis for hcp-Fe as a function of the temperature for the last 3.5 ps of simulation. In Fig. S1A the left vertical axis corresponds to the 8000 K simulation; the right vertical axis corresponds to the lower temperature simulations.
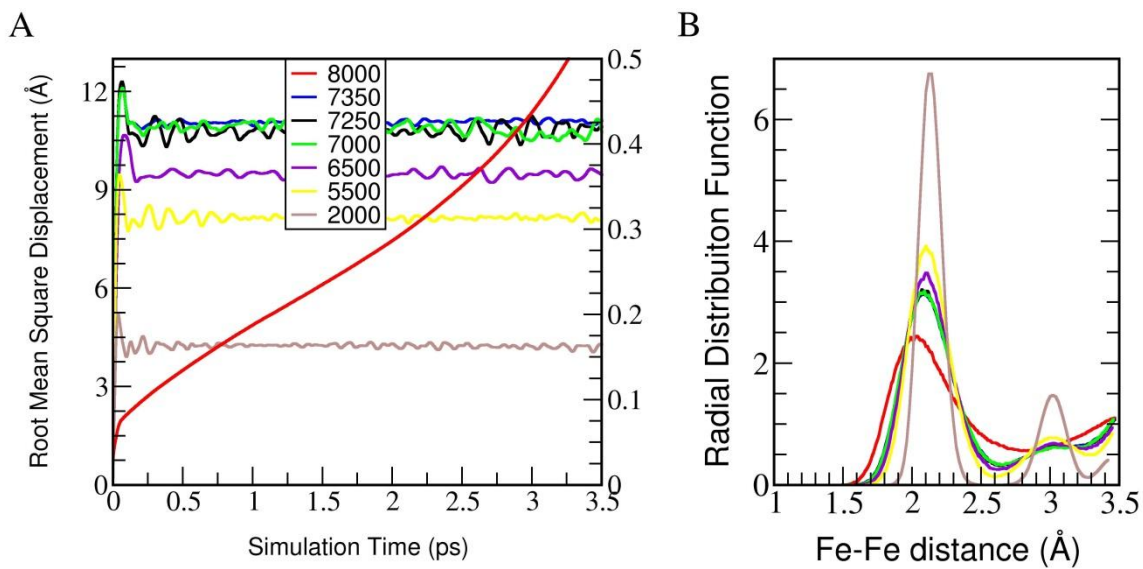
Fig. S2. Calculated shear modulus for hcp-Fe as a function of simulation temperature at 360 GPa. The black solid curve is a fit to the NP model (*19*) and the dashed line is the melting temperature obtained from this model. The grey band represents the minimum and maximum melting temperatures of hcp-Fe at 360 GPa (*18*).
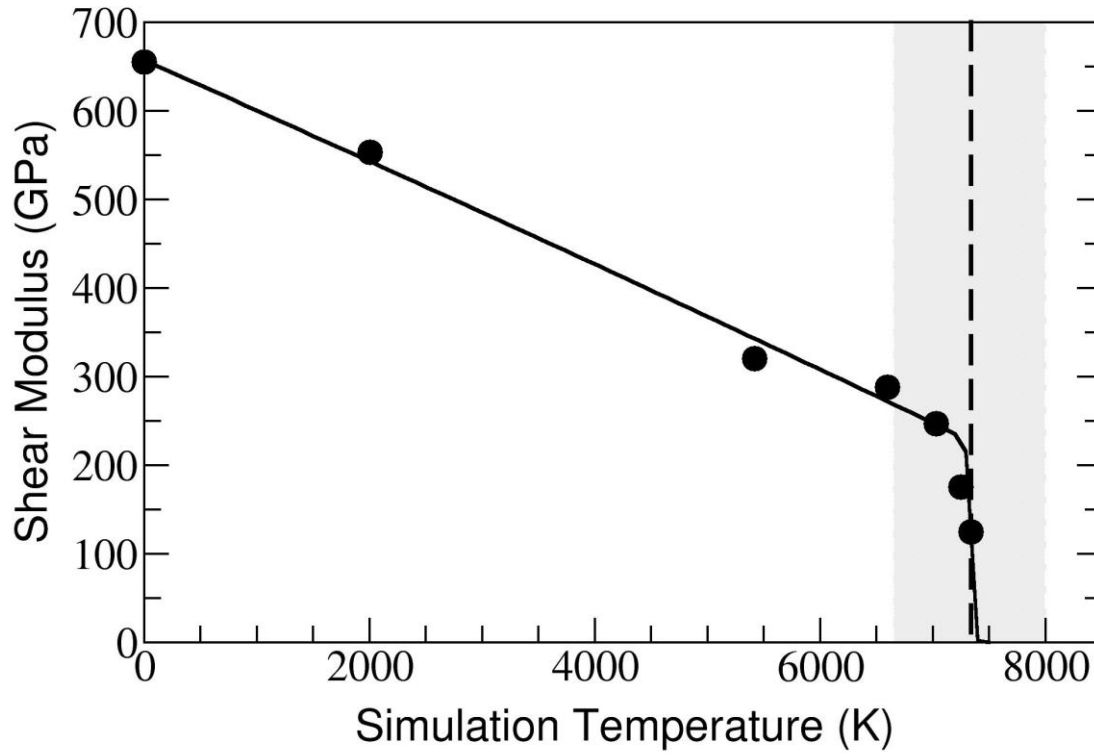
Fig. S3. Percentage of atomic defects in the hcp-Fe structure at 360 GPa as a function of temperature. The system melts when atomic defects are present in 40% of the system, indicated by the dashed.
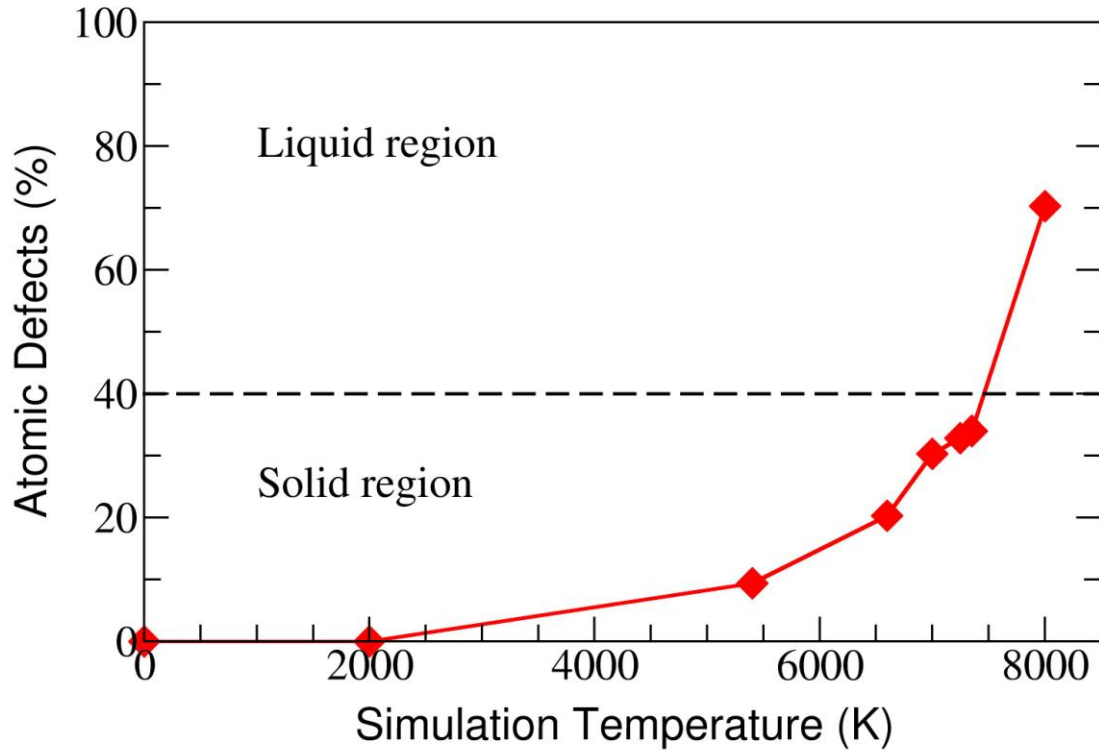
Table S1. Elastic properties and densities for hcp-Fe alloys and PREM at 360 GPa.

	T_{Final} (K)	ρ (kg m^{-3})	c_{11} (GPa)	c_{12}	c_{33}	c_{13}	c_{44}	K (GPa)	G	V_p (km s^{-1})	V_s
Fe	0[*]	14185	2493	1151	2689	1085	577	1590	655	13.18	6.80
	2000[*]	14138	2355	1282	2571	1083	476	1623	553	12.92	6.26
	5400[*]	13739	1924	1310	2108	1098	237	1560	320	12.05	4.83
	6600	13628	1814	1298	2063	1130	236	1562	288	11.90	4.58
	7000	13529	1710	1304	1882	1060	203	1481	247	11.57	4.24
	7250	13495	1424	1182	1822	1051	162	1384	181	10.99	3.67
	7340	13482	1167	1050	1784	1014	110	1253	125	10.26	3.04
PREM[†]		13090								11.26	3.67

[*] ref.*9*; † ref.*10* .